Automated Segmentation of Overlapping Cytoplasm in Cervical Smear Images via Contour Fragments

Youyi Song,[*] **Jing Qin,**[*] **Baiying Lei,**[§] **Kup-Sze Choi**[*]

[*]Center for Smart Health, School of Nursing, The Hong Kong Polytechnic University
[§]National-Regional Key Technology Engineering Laboratory for Medical Ultrasound, Guangdong Key Laboratory for Biomedical Measurements and Ultrasound Imaging, School of Biomedical Engineering, Shenzhen University, China
{youyi.song, harry.qin, thomasks.choi}@polyu.edu.hk and {leiby}@szu.edu.cn

Abstract

We present a novel method for automated segmentation of overlapping cytoplasm in cervical smear images based on contour fragments. We formulate the segmentation problem as a graphical model, and employ the contour fragments generated from cytoplasm clump to construct the graph. Compared with traditional methods that are based on pixels, our contour fragment-based solution can take more geometric information into account and hence generate more accurate prediction of the overlapping boundaries. We further design a novel energy function for the graph, and by minimizing the energy function, fragments that come from the same cytoplasm are selected into the same set. To construct the energy function, our fragments-based data term and pairwise term are measured from the spatial relation and shape prior, which offer more geometric information for the occluded boundary inference. Afterwards, occluded boundaries are inferred using the minimal path model, in which shape of each individual cytoplasm is reconstructed on the selected fragments set. Constructed shape is used as a constraint to locate the searching area, and curvature regulation is enforced to promote the smoothness of inference result. The inference result, in turn, is used as the shape prior to construct a high-level shape regulation energy term of the built graph, and then graph energy is updated. In other words, fragments selection and occluded boundary inference are iterative processed; this interaction makes more potential shape information accessible. Using two cervical smear datasets, the performance of our method is extensively evaluated and compared with that of the state-of-the-art approaches; the results show the superiority of the proposed method.

Introduction

Cervical cancer has a global health impact second in women (WHO 2013), and cytology-based screening is the most popular test in clinical to screen this disease at its early stage (Davey et al. 2006). But high expertise is required for manually screening, which is also a labor-intensive task (Kitchener et al. 2011); therefore, population-wide screening is still inaccessible in most developing countries (Saslow et al. 2012). To the end, automatic screening is highly demanded in clinical practice.
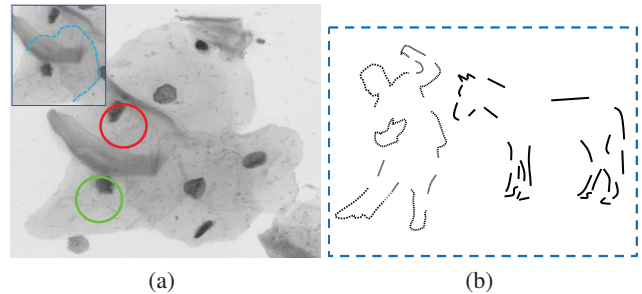
(a)　　　　　　　　　(b)

Figure 1: (a) Illustrate the strong intensity confusions in the occluded boundaries. Parts of the boundary of the cytoplasm indicated by the green circle is heavily occluded by the cytoplasm indicated by the red circle. Its ground truth is shown in the top left corner. (b) Illustrate our motivation of the proposed approach.

Accurate segmentation of cervical cells plays an essential role for the developing of the automatic screening system. Although extensive research has been devoted to this task (Kitchener et al. 2011; Guan, Zhou, and Liu 2015; Lu et al. 2017; Zhang et al. 2014; 2017a; Song et al. 2017; Tareef et al. 2017; Zhang et al. 2016), segmenting overlapping cytoplasm is still an open and challenging problem. The overlaps decrease intensity contrast or even hide partial boundaries of cytoplasm, which leads to difficulty of perceiving the whole boundary of each individual cytoplasm even for experienced histologists (an example is illustrated in Fig. 1 (a)).

In this paper, we present a novel algorithm for segmenting overlapping cervical cytoplasm. To better explain our motivation, please consider the image in Fig. 1 (b) where only parts of boundary information are given. It seems relatively easy for human to identify the whole object's boundary even though certain contour parts of the object are missing (Siddiqi, Tresness, and Kimia 1996). And intensity or color information seems to be not playing a significant role in this ability (De Winter and Wagemans 2004). Similarly, in our task, the occluded boundaries of cytoplasm can be regarded as the missing parts of contours, like those of the person or horse in the Fig. 1 (b).

To imitate this ability, first, we need to identify contour

parts of individual object from the image. For example, in the Fig. 1 (b), there are contour parts of a person and a horse, but when we attempt to identify the person we just take the contour parts of the person into consideration while excluding any part of the horse, and vice versa. The proposed method achieves this through two steps: fragments generation and fragments selection. Fragments generation cuts clumps' boundary into line segments (we refer to as fragments). This step is to identify the crossing points where different cytoplasm are meeting. Cutting clump boundary at these points can help to reduce the ambiguousness when identifying the contour parts of individual cytoplasm. Since a fragment with crossing points theoretically can belong to different cytoplasm, this step ensures each fragment only coming from one cytoplasm. Fragments selection groups fragments that come from the same cytoplasm, which is realized using a graph model. After that, we infer the gaps between two contour parts. The proposed method achieves this via finding a path connecting two neighboring fragments on which the designed energy function is minimized. Moreover, human seem to jointly identify contour parts and infer the gaps (Wagemans et al. 2012). Therefore, we use inference result as the shape constraint to reconstruct a high-level energy term into the graph and as the shape prior to update the graph's energy. We then select fragments again until the result of fragments selection is unaltered.

Related Work

Automatic cervical cancer screening has attracted a lot of computer researchers' interest and attention, and great advances have been made (Lu, Carneiro, and Bradley 2015; Zhang et al. 2016; Guan, Zhou, and Liu 2015; Zhang et al. 2014). This task generally consists of three steps. The first step is to segment cytoplasm and nuclei regions, assigning each pixel to background, cytoplasm, or nuclei regions. The second step is to segment overlapping cytoplasm, which is the task we address in this paper. The third step is to detect cancer cells as well as their cancerous stage. With the significant advance of machine learning techniques, especially the deep learning model, the first and third steps have obtained substantial progress (Song et al. 2015; Zhang et al. 2017a; 2017b; Taha, Dias, and Werghi 2017). However, most learning models cannot be directly applied to overlapping cytoplasm segmentation, in which pixels in the overlapping regions have to be given multiple outputs. For the same input sample, learning methods usually only can predict one reliable result.

Therefore, there are mainly two categories of methods to segment the overlapping cytoplasm. One is marker-controlled approaches (Sulaiman et al. 2010; Lee and Kim 2016; Plissiti, Vrikas, and Nikou 2015), including region growing or watershed. In these methods, nuclei are usually used as the markers, and then markers are growing until they are meeting. Therefore, this type of methods only can partition the overlapping regions; that is, they cannot provide any inference of occluded boundaries. Another type of approaches is level set-based models (Lu, Carneiro, and Bradley 2015; Song et al. 2017; Tareef et al. 2017; Nosrati and Hamarneh 2015; Song et al. 2016). These meth-

ods commonly resort to shape information, and certain inference of occluded boundaries can be accessible. Nonetheless, as the strong appearance confusions around the overlapping region and cytoplasm in the same clump often with different sizes, this type of methods is sensitive to the initialization. In addition, there is usually a great number of overlapping cytoplasm in a cervical smear image, level set-based methods thus demand heavy computational resource and time.

Contributions

Compared with most existing methods, the advantages of the proposed method are summarized below. (1) It directly works on fragments rather than pixels. Fragments not only can provide orientation and space relation information of cytoplasm, operating them as the basic processing units to represent cytoplasm outline also reduces the computational cost by several orders of magnitude. (2) In the inference of occluded boundaries, apart from appearance information, curvature regulation is also integrated into the new energy function of the minimal path model, and searching area is assumed around the boundary of its reconstructed shape. As a result, the negative effect caused by appearance distracters is largely minimized. (3) We incorporate the inference results as the shape constraint to correct the error in the fragments selection caused by the deficient observations of overlapped objects. With the sufficient interaction, certain potential cues are exploited, which compensate the deficiency of observations to some extent. Proposed approach has been tested on two cervical smear datasets with different staining ways. Its performance is also compared with several state-of-the-art methods. The proposed approach outperforms these methods in terms of both accuracy and computational efficiency.

Methodology

Fig. 2 illustrates the overview of the proposed approach. It begins with contour fragments generation, and then an undirected graph is established based on these fragments. We cluster these fragments, and infer the occluded boundaries simultaneously and interactively by minimizing the energy function of the undirected graph.

Fragments Generation

In order to generate the contour fragments, we first obtain the boundary of the whole cytoplasm clump and the nuclei using a multi-scale convolutional neural network (Song et al. 2015). We then obtain the initial set of contour fragments based on the following two steps. First, we compute the curvature of each point on the boundary of the whole cytoplasm, and set the points with the local extremum of curvature as the separation points between fragments, as these points are more likely located at the places where two cytoplasm meet. Second, due to the heavy overlapping of cytoplasm, it is difficult to distinguish all crossing points between cells only using curvature information. In this regard, we limit the length of each fragment to avoid that one fragment across two cells. In our implementation, we limit the length of each fragment to 30 pixels.
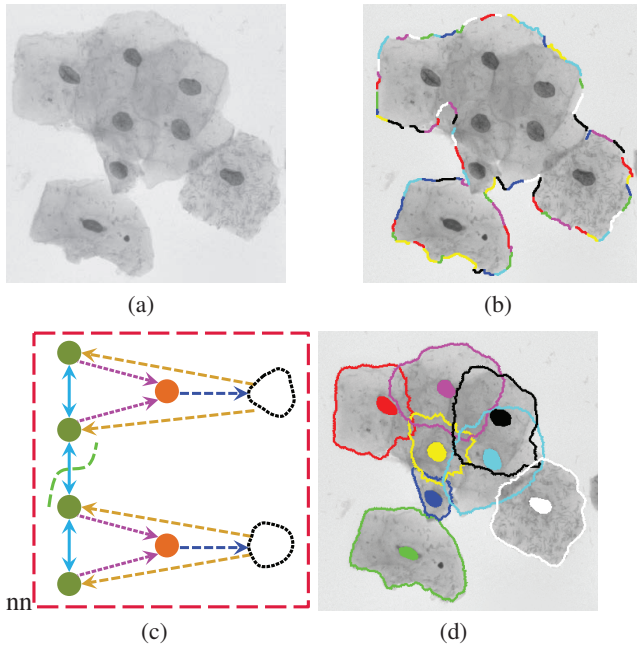
(a)　　　　　　　(b)

(c)　　　　　　　(d)

Figure 2: Illustration of the proposed approach. Given a source image (a), we generates the fragments (b) and establishes the graph, in which we jointly select the fragments' set and infer the occluded parts of the cytoplasm's boundary (c). In segmentation result (d), for the better viewing, nuclei are also depicted using the same color of its cytoplasm boundary.

Graph Construction

Once the contour fragments are generated, an undirected graph $\mathcal{G} = (\mathcal{V}, \mathcal{E})$ is established, where $\mathcal{V}$ represents the graph nodes and $\mathcal{E}$ is the graph edges connecting nodes. Our graph has three types of nodes. The first class of nodes is to represent contour fragments and we call them *F-node*. The *F-nodes* are connected by the *F-edges* in case that the two fragments are neighboring fragments. The second class of nodes is called *N-node*, which is used to denote the nuclei and initially connected to all the *F-nodes* in the same clump by the *N-edges*. The third class is called *T-node*, representing the terminal node of a clump, and each clump only has one terminal node. The *T-node* is also initially connected to all *F-nodes* in the clump. A graphical representation of our graph model is shown in Fig. 3.

In order to capture the probabilistic attributes of the fragments, we define the energy function of the graph as follows:

$$E(\mathbf{x}; \Psi) = \sum_{n \in N} \left(\sum_{i \in \mathcal{F}} \mathcal{L}_i(\mathbf{x}_i^n; \Psi^n) + \sum_{(i,j) \in \mathcal{N}_{\mathcal{F}}} \mathcal{L}_{ij}(\mathbf{x}_i^n, \mathbf{x}_j^n; \Psi^n) \right.$$
$$\left. + \mathcal{L}^n(\mathbf{x}^n; \Psi^n) \right), \qquad (1)$$

where $\mathcal{F}$ is the set of fragments and N is the set of nuclei in the image. The binary variables $\mathbf{x} \in \mathbb{B}^{\mathcal{F} \times N}$, we index as $\mathbf{x}_i^n$ over fragment $i \in \mathcal{F}$ and over nucleus $n \in N$, and we interpret $\mathbf{x}_i^n = 1$ to mean that fragment i comes from the cytoplasm with nucleus n. The notation $\mathbf{x}^n$ denotes fragments'

→ Occluded Boundaries Inference　--→ Shape Updating　⋯→ Energy Updating
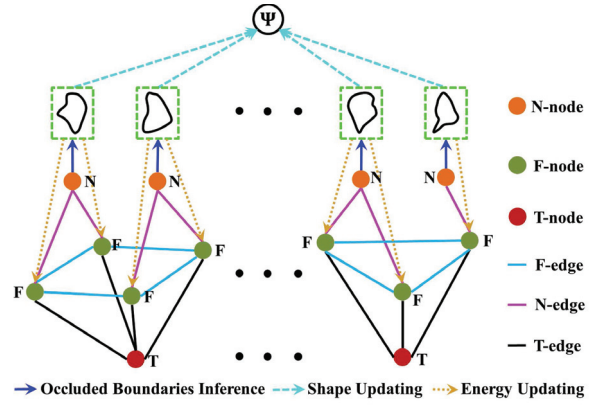
Figure 3: A graphical illustration of our graph model. For clarity, we only show the connections on two clumps, and assume left clump only having 4 fragments and 2 nuclei, while the right has 3 fragments and 2 nuclei.

set of the cytoplasm with the nucleus n. The shape parameter Ψ is initialized from the pre-trained shape reference, and then is updated from the inference results. The shape of cytoplasm with the nucleus n is represented as Ψ^n, consisting of the selected fragments' set $\mathbf{x}^n$ and the inference results among $\mathbf{x}^n$. The $\mathcal{N}_{\mathcal{F}}$ represents the spatial neighboring relation among fragments in the same clump; it is assumed as the nearest fragments measured using the minimal Euclidean distance among endpoints of the fragments. Each fragment therefore has two neighboring fragments.

The first energy term $\mathcal{L}_i(\mathbf{x}_i^n; \Psi^n)$ is usually called data term or unary term, measuring the cost of a fragment i coming from a cytoplasm with the nucleus n, encouraging agreements between an *N-node* corresponding to the nucleus n and the local evidence of fragment i. The second term $\mathcal{L}_{ij}(\mathbf{x}_i^n, \mathbf{x}_j^n; \Psi^n)$ is known as pairwise term, corresponding to the cost of assigning two neighboring fragments i and j to the same nucleus n, increasing the likelihood of that neighboring fragments i and j come from the same cytoplasm to be selected into the same group. The last term $\mathcal{L}^n(\mathbf{x}^n; \Psi^n)$ is the introduced high-level shape regulation energy term, prompting the consistency between inference results and the clump evidence, to encode the potential shape context into the graph by considering the space and shape cues of all cytoplasm in the clump.

Different with traditional graph models, in which shape parameter Ψ is accessible before the energy minimization, in our task, we have to estimate the shape parameter Ψ during the energy minimization. As shape parameter Ψ depends on the result of fragments selection, which is obtained after the minimizing of the graph's energy. In addition, with the new shape parameter Ψ, graph's energy is changed, and thus it has to be minimized again. That is to say, we are addressing the problem of jointly estimating $\mathbf{x}^*$, the optimal fragments selection, and Ψ^*, the optimal shape parameter:

$$\{\mathbf{x}^*, \Psi^*\} = \underset{\mathbf{x}, \Psi}{\operatorname{argmin}} E(\mathbf{x}; \Psi). \qquad (2)$$

Graph Energy Optimization

Energy terms computation: Our graph has three energy terms. The first term is the data term $\mathcal{L}_i(x_i^n; \Psi^n)$, and it is used for measuring the cost of a fragment i that belongs to the cytoplasm with the nucleus n. Our data term is derived from the combination of the space and shape constraints. It is observed that fragments usually have a relatively small space distance with the nucleus they come from, and also a relatively small shape distance with the shape of its cytoplasm.

Specifically, supposing that fragment i has m edge pixels, denoted by $e_i = \{p_1, \cdots, p_m\}$, the space distance with the nucleus n is measured as

$$g(i, n) = \min_{p_k \in e_i} g_k(p_k, n), \qquad (3)$$

where $g_k(p_k, n)$ is the Euclidean distance between edge pixel p_k and the centroid of nucleus n, if the line from the centroid to p_k entirely resides within the clump and if this line does not across other nuclei; otherwise, its value is set as ∞. The shape distance is counted as:

$$h(i, n) = \frac{1}{m} \sum_{p_k \in e_i} ||g_k(p_k, n) - g_k(p'_k, n)||, \qquad (4)$$

where p'_k is the corresponding boundary point with p_k in the Ψ^n, the estimated shape of cytoplasm with nucleus n. Consequently, our data term is obtained by summing these two items (both have been normalized to the range in $[0,1]$) with a balance parameter α, that is,

$$\mathcal{L}_i(x_i^n; \Psi^n) = \alpha g(i, n) + (1 - \alpha) h(i, n). \qquad (5)$$

The second term is the pairwise term $\mathcal{L}_{ij}(x_i^n, x_j^n; \Psi^n)$, which estimates how likely two neighboring fragments i and j come from the same cytoplasm. We use the same measure of the data term to compute it, but here i and j are treated as one new fragment ij, that is,

$$\mathcal{L}_{ij}(x_i^n, x_j^n; \Psi^n) = \alpha g(ij, n) + (1 - \alpha) h(ij, n). \qquad (6)$$

This measure is also effective for pairwise term computation. If two neighboring fragments do come from the same cytoplasm, the combined new fragment is like one with longer length, hence more evidences available to capture its probability distribution. By contrast, if they belong to different cytoplasm, there is no any shape fitting them both well, and they have two relatively equal space distances with their nuclei, so that there is a smaller value to any cytoplasm.

Throughout this paper, parameter α is set as 0.5 for equally weighting space and shape distances. And without the inference result, the shape parameter Ψ^n is unavailable. To address this, we select a set of manual labeled shape samples and then group them into K possible sets using k-means algorithm. And in each set, the sample with the minimal inner-class distance is selected as the shape reference. Next, shape distances between fragment i to all shape references are computed after the alignment. And the minimal shape distance is selected as the final shape distance of fragment i.

Third, the high-level shape regulation term $\mathcal{L}^n(x^n; \Psi^n)$, it is a clump-level constraint, and is to constrain the segmenting result. That is, the segmented result cannot overflow the clump, and at the same time all pixels in the clump have to be contained at least one cytoplasm. Therefore, it is defined as:

$$\mathcal{L}^n(x^n; \Psi^n) = \xi \text{card}(\cup_{n \in N}\Psi^n \setminus \mathbb{C} + \mathbb{C} \setminus \cup_{n \in N}\Psi^n), \quad (7)$$

where $\mathbb{C}$ represents the set of pixels in the clump. $\cup_{n \in N}\Psi^n \setminus \mathbb{C}$ is the set of background pixels that are segmented into certain cytoplasm. This error is caused in the occluded boundaries inference in which these background pixels are wrongly recognized as the cytoplasm pixels. Inversely, $\mathbb{C} \setminus \cup_{n \in N}\Psi^n$ is the set of those cytoplasm pixels that are segmented into background pixels after the inference process. And card represents the number of elements in a set, while ξ is the parameter to control the rate of the cost penalty.

Energy optimization: To minimize the energy of our graph, we first compute pairwise term to assign *F-edges* and data term to assign the *N-edges* and *T-edges*. Different with traditional graph model, our *T-edge* is assigned as

$$\mathcal{W}_{i,T} = \max_{n' \in N \setminus \{n\}} \mathcal{L}_i(x_i^{n'}; \Psi^{n'}), \qquad (8)$$

that is, the maximal value of data term of fragment i with all nuclei but n in the clump. Then, an expanded min-cut solution (Delong et al. 2012) is implemented to optimize graph's energy, which aims to assign each fragment to its cytoplasm. Based on the selected fragments of cytoplasm with the nucleus n, occluded boundaries inference is then implemented to obtain its new shape parameter Ψ^n. Once the shape parameter is updated, we update graph's energy terms and optimize it again until the selection result is stable.

Occluded Boundaries Inference

In order to infer the occluded boundary parts of each individual cytoplasm, we first reconstruct its shape using the selected fragments. Although reconstructed shape has certain shape loss in local details, it can provide the rough position of those occluded boundaries. We hence use it as a constraint of our minimal path model, to narrow the searching area of the path.

Specifically, we first compute the mean shape μ_s and the covariance matrix $\sum_s$ of the selected manual labeled shape samples, and we assume any new reconstructed shape $\mathcal{C}$ following a Gaussian distribution with μ_s and $\sum_s$, that is,

$$\mathcal{C} \approx \mu_s + \lambda b, \qquad (9)$$

where λ is the eigenvectors of $\sum_s$, and b is the projection vector of $\mathcal{C}$ onto the principle components in shape space Ω_{R^2}. Under this assumption, given a selected fragments set x^n, its corresponding location on its shape $\mathcal{C}_n$ represents L_n, the shape reconstruction problem can be formulated through finding the most probable compete shape $\mathcal{C}_n^*$, that is,

$$\mathcal{C}_n^* = \underset{\mathcal{C}_n \in \Omega_{R^2}}{\text{argmax}}\, p(\mathcal{C}_n | x^n, L_n; \mu_s, \textstyle\sum_s). \qquad (10)$$

Due to the complexity of computing Eqn. 10, we implement this Maximum a Posterior problem by finding the optimal projection vector b_n^*, that is,

$$b_n^* = \underset{b_n \in \Omega_{R^2}}{\text{argmax}}(b_n^T \textstyle\sum_s^{-1} b_n + \omega ||L'_n + \lambda' b_n - x^n||), \quad (11)$$

where b_n^T and $\sum_s^{-1}$ are the transpose of b_n and the inverse matrix of $\sum_s$, respectively. And L'_n is the corresponding location of L_n on the mean shape, while λ' is the corresponding submatrix of λ. The weight parameter ω is to balance

the global prior and local observation. The global prior is to constrain $\mathbf{x}^n$ close to the mean shape μ_s as much as possible, while the local observation is for prompting the matching accuracy between $\mathbf{x}^n$ and its corresponding location L'_n. Eqn. 11 is then approached by the approach described in (Duchi et al. 2008). And, once b_n^* is obtained, the shape $\mathcal{C}_n^*$ is reconstructed using the Eqn. 9.

We now present how to infer the gaps between two neighboring fragments. For an arbitrary pair of neighboring fragments, two endpoints that the path γ travelling are denoted as p_s and p_e, the best inference of the gap is assumed when

$$\mathbb{E}(\gamma) = \min_{\gamma \in p_s \rightarrow p_e} \int_\gamma f(\gamma(s))ds, \qquad (12)$$

where s is the arc length parameter, and f is the potential function that takes a lower value when γ near the real path. In this paper, potential function f is integrated with the color cues, shape cues and the curvature regulation, that is,

$$f(\gamma(s)) = -\omega_1||\nabla I(s)|| + \omega_2||\nabla\mathcal{C}(s)|| + k^2(s), \quad (13)$$

where $||\nabla I||$ is the gradient magnitude of intensity at the arc s, while $||\nabla\mathcal{C}||$ is the pixel-wise distance between s and the boundary of the reconstructed shape $\mathcal{C}$. And we only search the points where $||\nabla\mathcal{C}|| < 10$ to exclude the intensity noisy points. k represents the curvature, while ω_1 and ω_2 are the proportionality constants.

As Eqn. 13 is not a first-order non-linear partial differential equation, Eqn. 12 does not satisfy the Eikonal equation, so traditional minimal path model is unable to optimize the Eqn. 12. However, in the image plane, the path from p_s to p_e consists of the pairs of neighboring pixel points. In other words, the point at the path γ must be connected with its neighboring points. Therefore, we approach Eqn. 12 via first computing the minimal action map using a front propagation from p_s to p_e and then a back propagation from p_e to p_s only considering the neighboring points.

Once the inference is finished, graph's energy is updated and we begin to optimize the graph again until the result of fragments selection is stable.

Experiment

Datasets

To evaluate the effectiveness of the proposed approach, we conduct experiments on two cervical smear datasets with different stains. One is prepared by Papanicolaou (Pap) stain and the stack data have been converted into the Extended Depth of Field (EDF) images. This dataset is obtained from the website of *ISBI* 2015 Overlapping Cervical Cytology Image Segmentation Challenge. For 8 public available images, there are 20$\sim$60 cells in each of them, distributing 11 clumps with 3.3 cells per clump on average. Another dataset is stained by Hematoxylin and Eosin (H&E), collected from Shenzhen Sixth People's Hospital, Shenzhen, China; consists of 21 images with 30$\sim$80 cells per image, distributing 7 clumps with 6.1 cells per clump on average.

Evaluation Metrics

A commonly used metric to evaluate segmentation performance is the Dice similarity coefficient which measures the similarity of two binary regions as: $DC = 2|R_s \cap R_g|)/(|R_s|+|R_g|)$ (R_s and R_g denote the segmented region and its ground truth). However, this is an area-based metric; it is less likely to measure the shape similarity. Hence, we add two metrics based on shape smoothness $\mathcal{S}(R)$ and roundness $\mathcal{O}(R)$ computed as

$$\mathcal{S}(R) = \oint_{p \in \partial R} |d\theta(p)|, \qquad (14)$$

$$\mathcal{O}(R) = \int_{p \in R} dp/(\oint_{p \in \partial R} dp)^2, \qquad (15)$$

where ∂R is the boundary of region R, while θ and $|\cdot|$ represent the change of the tangent angle at boundary point p and absolute value. These two terms characterize non-concave degree and compactness of the region shape respectively, and are invariant to scaling and rotation. The smoothness similarity coefficient SC and roundness similarity coefficient RC are then defined as

$$SC = 1 - |\mathcal{S}(R_s) - \mathcal{S}(R_g)|/\mathcal{S}(R_g), \qquad (16)$$

$$RC = 1 - |\mathcal{O}(R_s) - \mathcal{O}(R_g)|/\mathcal{O}(R_g). \qquad (17)$$

In addition, we also use true positive rate TPR to evaluate the performance, and here it is computed as $TPR = |R_s \cap R_g|/(|R_s \cap R_g| + |R_g \setminus R_s \cap R_g|)$.

Parameters Selection

The proposed method has four parameters: penalty rate ξ in Eqn. 7, weight parameter ω in Eqn. 11, and two proportionality constants ω_1 and ω_2 in Eqn. 13. All these four parameters are optimized by the cross validation procedure on a small training dataset, and our experimental findings of these parameters are follows.

When using a small value of penalty rate ξ, the role of this energy term is diminished; however, when using a large value of it, it is more likely to lead to turbulence of graph's energy, so that graph's convergence cannot be reached. It is set as 1.5 in both datasets. The value of ω roughly depends on the overlapping degree in the dataset; the higher overlapping degree, the larger value. In our experiments, we set it to 7 in the Pap stain dataset, and to 10 in the H&E dataset. The values of ω_1 and ω_2 rely on imaging quality and overlapping degree. When images with high imaging quality and low overlapping degree, they both should be set a larger value; otherwise, curvature's role should be stressed greater. They are set as 1 and 0.2 in the Pap dataset, and as 0.7 and 0.4 in the H&E dataset, respectively.

Comparisons

To evaluate proposed method, we employ six algorithms on both datasets for comparison. We implemented approaches reported in (Lu, Carneiro, and Bradley 2015) and in (Song et al. 2017), and they are termed as LSF and MCL in this paper respectively. We also conduct experiments to demonstrate the importance of color cues, shape cues, and curvature regulation in our task by only using one of them to infer occluded boundaries, termed as CS-A, CS-S and CS-K, respectively. The importance of joint selecting fragments and inferring occluded boundaries is also demonstrated; in this

experiment, inference result does not be returned to guide fragments' selection, called as CS-1.

Results

Table 1 summaries the performance of comparisons according to overlapping degree. The overlapping degree is measured according to the ratio of occluded boundaries' length against the length of the object"s whole boundary. Note that the number of cytoplasm in the clump is not a direct factor of evaluating the algorithms' performance. Although performance is generally worse with the increasing of the number of cytoplasm, it is more a matter of overlapping degree increasing in this case. Therefore, performance reported in Table 1 is organised by overlapping degree rather than the number of cytoplasm in the clump.

According to Table 1, performance of all methods decreases with the increasing of overlapping degree. All these algorithms seem to be insensitive of test dataset; dominant performance in either dataset has not been observed. The performance difference among comparisons is also not significant when overlapping degree less than 0.3, but the performance of proposed approach becomes superior to others with the increasing of overlapping degree. Compared with LSF and MCL, proposed approach obtains an obvious performance improvement, except for RC result when overlapping degree is with a small value. CS-S gets a slightly better performance than CS-A, while their performances are both not exceeding ours in the most cases. Although CS-K and CS-1 have similar results with ours when overlapping degree less than 0.3, the proposed method acquires a competitive results against theirs when cytoplasm are overlapping more heavily.

For better comparing the proposed method with different approaches and discussing the reasons causing the differences among them, some result samples are selected in Fig. 4. The first row is a sample where overlapping cytoplasm are with different sizes. LSF is affected by the noise indicated by red arrow, while MCL and CS-A get the unnatural boundaries. The second and fourth rows are the samples in which the number of cytoplasm is over 6 and some of them are heavily overlapped. With the increasing of the number of cytoplasm in the clump, LSF shows the unnatural results, while the results of MCL shows sufficient smoothness, shape similarity coefficients SC and RC are lower. CS-A and CS-K also only get a coarse result. CS-1 and ours have similar results, but when cytoplasm is occluded more and the fragments are less discriminative (see these cells indicted by red arrows), CS-1 shows its inability in this case. The sample in third row is with lower color contrast affected by poor illumination. MCL and CS-A only show limited shape capture ability, while the result of LSF tends to be an ellipse. CS-K also shows this tend when cytoplasm are overlapping very heavy (see the cell indicted by red arrow in the third row).

All experiments are conducted on a PC with a 2.20 GHz Intel Core i5 CPU and 4.00 GB of RAM, and they are all implemented in MATLAB. The processing time is related to the number of cells in the clump. We found that, for a clump with 5 cells, the average processing times are 12 minutes of LSF, 8 minutes of MCL, and 5 minutes of proposed method, respectively. Therefore, computational efficiency of the proposed method also outperforms that of previous approaches.

Conclusion

For automatic screening of cervical cancer, accurate segmentation of cervical cells is required. However, cytoplasm overlapping makes the observation of each individual cytoplasm deficient, hindering the identification of the whole boundary. In this paper, we have presented a method to segment overlapping cytoplasm via exploring the contour fragments, which offers more geometric information than pixels. In order to segment individual cytoplasm from the clump, it groups fragments that come from the same cytoplasm using an undirected graph. It then resorts to statistical shape model and minimal path theory to infer the occluded boundaries of cytoplasm. We have also demonstrated its capability, and compared its performance with the related approaches. The experimental results show that our method achieves the obvious improvement in terms of both segmentation accuracy and computational efficiency in comparison with previous methods.

References

Davey, E.; Barratt, A.; Irwig, L.; Chan, S. F.; Macaskill, P.; Mannes, P.; and Saville, A. M. 2006. Effect of study design and quality on unsatisfactory rates, cytology classifications, and accuracy in liquid-based versus conventional cervical cytology: a systematic review. *The Lancet* 367(9505):122–132.

De Winter, J., and Wagemans, J. 2004. Contour-based object identification and segmentation: Stimuli, norms and data, and software tools. *Behavior Research Methods, Instruments, & Computers* 36(4):604–624.

Delong, A.; Osokin, A.; Isack, H. N.; and Boykov, Y. 2012. Fast approximate energy minimization with label costs. *International journal of computer vision* 96(1):1–27.

Duchi, J.; Shalev-Shwartz, S.; Singer, Y.; and Chandra, T. 2008. Efficient projections onto the l 1-ball for learning in high dimensions. In *Proceedings of the 25th international conference on Machine learning*, 272–279. ACM.

Guan, T.; Zhou, D.; and Liu, Y. 2015. Accurate segmentation of partially overlapping cervical cells based on dynamic sparse contour searching and gvf snake model. *IEEE journal of biomedical and health informatics* 19(4):1494–1504.

Kitchener, H. C.; Blanks, R.; Dunn, G.; Gunn, L.; Desai, M.; Albrow, R.; Mather, J.; Rana, D. N.; Cubie, H.; Moore, C.; et al. 2011. Automation-assisted versus manual reading of

Table 1: Splitting results of the algorithms according to overlapping degree

| | Overlapping Degree $\in (0, 0.3]$ | | | | | | | | Overlapping Degree $\in (0.3, 0.6]$ | | | | | | | | Overlapping Degree $\in (0.6, 1)$ | | | | | | | |
| | Pap Stain | | | | H&E Stain | | | | Pap Stain | | | | H&E Stain | | | | Pap Stain | | | | H&E Stain | | | |
	TPR	DC	SC	RC	TPR	DC	SC	RC	TPR	DC	SC	RC	TPR	DC	SC	RC	TPR	DC	SC	RC	TPR	DC	SC	RC
LSF	0.78	0.80	0.75	0.89	0.76	0.79	0.77	0.89	0.76	0.77	0.80	0.86	0.74	0.75	0.77	0.83	0.70	0.73	0.75	0.82	0.67	0.69	0.72	0.80
MCL	0.76	0.79	0.81	**0.92**	0.77	0.80	0.83	**0.90**	0.74	0.78	0.83	0.88	0.72	0.74	0.82	0.84	0.72	0.75	0.76	0.83	0.70	0.73	0.73	0.82
CS-A	0.77	0.79	0.73	0.83	0.79	0.81	0.74	0.84	0.73	0.76	0.82	0.84	0.75	0.78	0.80	0.82	0.69	0.72	0.73	0.81	0.68	0.71	0.71	0.81
CS-S	0.77	0.79	0.77	0.88	0.78	0.81	0.77	0.87	0.76	0.77	0.83	0.86	0.73	0.75	0.82	0.84	0.69	0.72	0.76	0.82	0.68	0.71	0.74	0.82
CS-K	0.79	0.82	0.82	0.90	0.80	0.82	0.81	0.89	0.75	0.78	0.81	0.85	0.74	0.76	0.81	0.83	0.67	0.70	0.72	0.79	0.64	0.68	0.70	0.77
CS-1	0.77	0.80	0.83	0.84	0.78	0.81	0.83	0.85	0.74	0.77	0.79	0.83	0.75	0.77	0.81	0.84	0.67	0.71	0.73	0.82	0.68	0.70	0.71	0.81
Ours	**0.82**	**0.84**	**0.87**	0.91	**0.80**	**0.83**	**0.85**	0.89	**0.80**	**0.82**	**0.84**	**0.89**	**0.77**	**0.80**	**0.83**	**0.86**	**0.78**	**0.80**	**0.77**	**0.85**	**0.76**	**0.78**	**0.75**	**0.83**
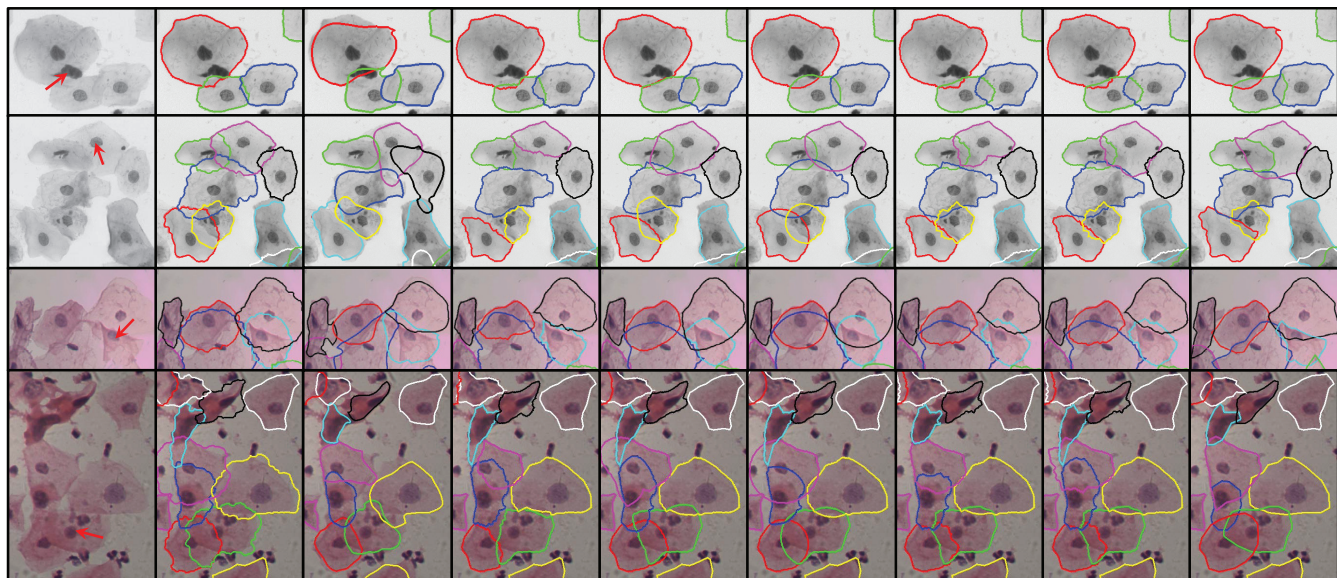
Figure 4: Result samples, first tow rows come from Pap stain dataset, while last two rows are from H&E stain dataset. From left to right column: source images, results of LSF, MCL, CS-A, CS-S, CS-K, CS-l, and ours, respectively, and ground truth. Note that samples' sizes have been scaled for better viewing.

cervical cytology (mavaric): a randomised controlled trial. *The lancet oncology* 12(1):56–64.

Lee, H., and Kim, J. 2016. Segmentation of overlapping cervical cells in microscopic images with superpixel partitioning and cell-wise contour refinement. In *Proceedings of the IEEE Conference on Computer Vision and Pattern Recognition Workshops*, 63–69.

Lu, Z.; Carneiro, G.; Bradley, A. P.; Ushizima, D.; Nosrati, M. S.; Bianchi, A. G.; Carneiro, C. M.; and Hamarneh, G. 2017. Evaluation of three algorithms for the segmentation of overlapping cervical cells. *IEEE journal of biomedical and health informatics* 21(2):441–450.

Lu, Z.; Carneiro, G.; and Bradley, A. P. 2015. An improved joint optimization of multiple level set functions for the segmentation of overlapping cervical cells. *IEEE Transactions on Image Processing* 24(4):1261–1272.

Nosrati, M. S., and Hamarneh, G. 2015. Segmentation of overlapping cervical cells: A variational method with star-shape prior. In *Biomedical Imaging (ISBI), 2015 IEEE 12th International Symposium on*, 186–189. IEEE.

Plissiti, M. E.; Vrigkas, M.; and Nikou, C. 2015. Segmentation of cell clusters in pap smear images using inten-

sity variation between superpixels. In *Systems, Signals and Image Processing (IWSSIP), 2015 International Conference on*, 184–187. IEEE.

Saslow, D.; Solomon, D.; Lawson, H. W.; Killackey, M.; Kulasingam, S. L.; Cain, J.; Garcia, F. A.; Moriarty, A. T.; Waxman, A. G.; Wilbur, D. C.; et al. 2012. American cancer society, american society for colposcopy and cervical pathology, and american society for clinical pathology screening guidelines for the prevention and early detection of cervical cancer. *CA: a cancer journal for clinicians* 62(3):147–172.

Siddiqi, K.; Tresness, K. J.; and Kimia, B. B. 1996. Parts of visual form: Psychophysical aspects. *Perception* 25(4):399–424.

Song, Y.; Zhang, L.; Chen, S.; Ni, D.; Lei, B.; and Wang, T. 2015. Accurate segmentation of cervical cytoplasm and nuclei based on multiscale convolutional network and graph partitioning. *IEEE Transactions on Biomedical Engineering* 62(10):2421–2433.

Song, Y.; Cheng, J.-Z.; Ni, D.; Chen, S.; Lei, B.; and Wang, T. 2016. Segmenting overlapping cervical cell in pap smear images. In *Biomedical Imaging (ISBI), 2016 IEEE 13th International Symposium on*, 1159–1162. IEEE.

Song, Y.; Tan, E.-L.; Jiang, X.; Cheng, J.-Z.; Ni, D.; Chen, S.; Lei, B.; and Wang, T. 2017. Accurate cervical cell segmentation from overlapping clumps in pap smear images. *IEEE transactions on medical imaging* 36(1):288–300.

Sulaiman, S. N.; Isa, N. A. M.; Yusoff, I. A.; and Othman, N. H. 2010. Overlapping cells separation method for cervical cell images. In *Intelligent Systems Design and Applications (ISDA), 2010 10th International Conference on*, 1218–1222. IEEE.

Taha, B.; Dias, J.; and Werghi, N. 2017. Classification of cervical-cancer using pap-smear images: A convolutional neural network approach. In *Annual Conference on Medical Image Understanding and Analysis*, 261–272. Springer.

Tareef, A.; Song, Y.; Cai, W.; Huang, H.; Chang, H.; Wang, Y.; Fulham, M.; Feng, D.; and Chen, M. 2017. Automatic segmentation of overlapping cervical smear cells based on local distinctive features and guided shape deformation. *Neurocomputing* 221:94–107.

Wagemans, J.; Elder, J. H.; Kubovy, M.; Palmer, S. E.; Peterson, M. A.; Singh, M.; and von der Heydt, R. 2012. A century of gestalt psychology in visual perception: I. perceptual grouping and figure–ground organization. *Psychological bulletin* 138(6):1172.

WHO. 2013. Information centre on hpv and cervical cancer (hpv information centre), human papillomavirus and related diseases report in china. [online]. available: www.who.int/hpvcentre.

Zhang, L.; Kong, H.; Ting Chin, C.; Liu, S.; Fan, X.; Wang, T.; and Chen, S. 2014. Automation-assisted cervical cancer screening in manual liquid-based cytology with hematoxylin and eosin staining. *Cytometry Part A* 85(3):214–230.

Zhang, J.; Hu, Z.; Han, G.; and He, X. 2016. Segmentation of overlapping cells in cervical smears based on spatial relationship and overlapping translucency light transmission model. *Pattern Recognition* 60:286–295.

Zhang, L.; Lu, L.; Nogues, I.; Summers, R.; Liu, S.; and Yao, J. 2017a. Deeppap: Deep convolutional networks for cervical cell classification. *IEEE Journal of Biomedical and Health Informatics*.

Zhang, L.; Sonka, M.; Lu, L.; Summers, R. M.; and Yao, J. 2017b. Combining fully convolutional networks and graph-based approach for automated segmentation of cervical cell nuclei. In *Biomedical Imaging (ISBI 2017), 2017 IEEE 14th International Symposium on*, 406–409. IEEE.